JOURNAL OF COMPUTATIONAL AND THEORETICAL TRANSPORT
https://doi.org/10.1080/23324309.2020.1843496

On the Ronen Method in Simple 1-D Geometries for Neutron Transport Theory Solutions

Daniele Tomatis[a], Roy Gross[b], and Erez Gilad[b]

[a]DES, Service d'études des réacteurs et de mathématiques appliquées (SERMA), CEA, Université Paris-Saclay, Gif-sur-Yvette, France; [b]The Unit of Nuclear Engineering, Ben-Gurion University of the Negev, Beer-Sheva, Israel

ABSTRACT

In this work, we apply the Ronen method to obtain highly-accurate approximations to the solution of the neutron transport equation in simple homogeneous problems. Slab, cylindrical, and spherical geometries are studied. This method demands successive resolutions of the diffusion equation, where the local diffusion constants are modified in order to reproduce new estimates of the currents by a transport operator. The diffusion solver employs here finite differences and the transport-corrected currents are forced in the numerical scheme by means of drift terms, like in the CMFD scheme. Boundary conditions are discussed introducing proper approximations to save the particle balance in case of reflection in the slab. The solution from the Ronen iterations is compared against reference results provided by the collision probability method. More accurate estimates of the currents are provided by integral transport equations using first flight escape probabilities. Slow convergence on the scalar flux is analyzed, although the results match the reference solutions in the limit of fine meshes and far from the bare boundary.

KEYWORDS

Ronen method; collision probability method; neutron transport; CMFD

1. Introduction

In 2004, Ronen suggested to calculate more accurate currents by means of an integral transport operator still using a neutron flux computed in diffusion theory (Ronen 2004). This allowed having new estimates of the diffusion coefficient still using Fick's law. Since these estimates need a known flux distribution, it was also suggested to execute new diffusion calculations, thus updating iteratively the diffusion coefficient in the global calculation. The main reason motivating this method was to overcome the underlying limitation of Fick's law requiring low flux gradients, and so low neutron absorption and high scattering in general. Nevertheless, isotropic scattering remained as a basic postulate.

CONTACT Daniele Tomatis daniele.tomatis@cea.fr DES, Service d'études des réacteurs et de mathématiques appliquées (SERMA), CEA, Université Paris-Saclay, F-91191 Gif-sur-Yvette, France.

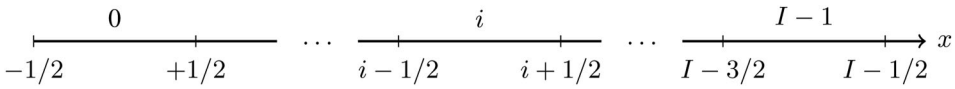

Figure 1. Notation of the 1D mesh.

This idea was later used by Tomatis and Dall'Osso, who provided a numerical demonstration in a simple slab problem (Tomatis and Dall'Osso 2011). Instead of updating the diffusion coefficient by the ratio of the current exchange and the flux gradient, as in Fick's law, they recurred to the scheme of the coarse mesh finite differences (CMFD) method for taking into account the new currents estimated by the integral transport operator in the diffusion solver. This technique, largely adopted in the literature of nodal methods (Smith 1983; Lawrence 1986), can avoid indeterminate divisions in case of vanishing current and flux gradient. They tested this implementation in a bare slab with two-group cross sections homogenized in a realistic PWR assembly. It was observed that the Ronen method (RM) could drive the flux from diffusion towards the reference of the integral Boltzmann transport equation, regardless of the initial formulation used for the diffusion coefficient. Remarkably, the unphysical zero-flux boundary condition was not preventing to correct the flux near the boundary, that is within a few mean free paths. However, higher errors were noticed at the boundary with vacuum, slowly decreasing even after many iterations.

In this work, we investigate further the convergence on the first flux moments, aiming to extend the study to the cylindrical and spherical geometries with homogeneous media. The details of the implementation of the RM in the diffusion solver are presented in Section 2, while the procedure to estimate the currents by the integral transport operator follows in Section 3. Boundary conditions are derived in Section 4. The results on a few characteristic configurations are discussed in Section 5. Finally, the article ends with the conclusion in Section 6.

2. Implementation

The cross sections, as well as the diffusion coefficient, are usually available as volume-averaged data per cell in the mesh. A lattice transport computer code can prepare these data by homogenization. Once the scalar flux is known from the finite differences solver using the original diffusion coefficients, the integral expressions derived in Section 3 can be used to get new estimates of the current J at the cell interfaces. Instead of computing new diffusion coefficients on the same interfaces straight by Fick's law, $J = -D\partial_x\phi$, we obtain new corrective currents $\delta J = J - \Upsilon$ that are supplied next to the neutron balance in diffusion. Here, Υ is the current obtained with the original values of the diffusion coefficient and with the derivative

approximated by finite differences. In 1D geometry and using the notation in Figure 1, it is:

$$\Upsilon_{i+1/2} = -2D_{i+1/2}\frac{\phi_{i+1} - \phi_i}{\Delta_{i+1} + \Delta_i}, \text{ for } i = 0, ..., I-1, \tag{1}$$

where $\Delta_i = (x_{i+1/2} - x_{i-1/2})$. Integer and rational subscripts indicate cell-averaged and interface quantities, respectively. Since the input diffusion coefficients are provided as volume-averaged, and that they are always needed at interfaces, we approximate them by local volume averages:

$$D_{i+1/2} = \frac{D_{i+1}V_{i+1} + D_iV_i}{V_{i+1} + V_i}, \text{ for } i = 0, ..., I-1. \tag{2}$$

The values of the diffusion coefficient at $-1/2$ and $I-1/2$ are simply the coefficients of the boundary cells. V_i is the reduced volume in the i-th cell, that is determined along the only dimension of interest. It is then per unit of transverse surface in the slab, the unit azimuthal angle in the cylinder and per unit cone in the sphere. Specifically, $V_i = \Delta_i c_i$ with c_i depending on the system of coordinates. The c coefficients are unitary in the Cartesian frame. In the cylinder, $c_i = x_i$ for all i with $x_i = (x_{i-1/2} + x_{i+1/2})/2$ (arithmetic mean), whereas $c_i = (4x_i^2 - \hat{x}_i^2)$ in the sphere with $\hat{x}_i = \sqrt{x_{i-1/2}x_{i+1/2}}$ (geometric mean). The discretized form of the current δJ must involve the flux in order to be taken into account in the finite differences' equations. Its representation is changed into a drift-advection term determined by the neighboring cell fluxes, thus avoiding possible undefined division by zeros in case of flat flux (Smith 1983):

$$\delta J_{i+1/2} = -2\delta D_{i+1/2}\frac{\phi_{i+1} + \phi_i}{\Delta_{i+1} + \Delta_i}, \text{ for } i = 0, ..., I-1. \tag{3}$$

This allows determining the new numerical corrections δD to use in the finite differences solver, together with the diffusive currents from Equation (1). If necessary, the spatial differences at the denominator of Equation (3) can be removed by reason of the arbitrary definition used for δD. Finally, the neutron balance resolved by the CMFD takes into account both types of currents Υ and δJ. Non-linear iterations with new corrections given by δJ are needed because of their dependence on the unknown flux.

The divergence operator used in the multi-group balance equation can be described with the general form $d_x(x^b J_g)/x^b$, with $b = 0$, 1, and 2 respectively for the slab, for the cylinder, and for the sphere. We solve then for the volume-integrated flux,

$$\hat{\phi}_{g,i} = \int_{x_{i-1/2}}^{x_{i+1/2}} x^b \phi_g(x) dx = \bar{\phi}_{g,i} V_i,$$

making the approximation that the average group flux $\bar{\phi}_{g,i} \approx \phi_{g,i}$ in the equations above.

3. Current estimation

3.1. Slab geometry

The angular flux from the integral transport equation (with standard notation) is:

$$\varphi(x,\mu) = \varphi(x_b,\mu)e^{-\tau(x_b,x)/\mu} + \int_{x_0}^{x} dx' \frac{q(x',\mu)}{\mu} e^{-\tau(x',x)/\mu}, \tag{4}$$

with the optical length

$$\tau(x_1,x_2) = \int_{x_1}^{x_2} dx' \sigma_t(x').$$

Contrary to other formulations, we do not include the direction cosine of the neutron velocity μ in the definition of the optical length to ease the numerical integrations in the following. Equation (4) holds for both positive directions $(\mu > 0)$ where $x_0 = x_{-1/2} = a$, and negative ones $(\mu > 0)$ where $x_0 = x_{I-1/2} = b$. The inclusion of the energy variable in Equation (4) is straightforward; we use hereafter the multi-group theory, writing the source q_g as[1]:

$$q_g = \sum_{g'=1}^{G} \left[\sum_{l=0}^{\infty} \frac{2l+1}{2} \sigma_{s,l,g'\to g}(x) P_l(\mu) \varphi_{l,g'}(x) + \frac{\chi_g}{2\{k\}} \nu\sigma_{f,g'}(x)\phi_{g'}(x) \right] + S_g, \tag{5}$$

where the subscript l refers to the moments of the expansions of the flux and of the scattering cross section on the Legendre polynomials P_l. Fission emission is isotropic, so that only the scalar flux ϕ being equal to the first moment φ_0 is retained for the fission term. Without the external source S, the multiplication factor k is used as eigenvalue to avoid the only trivial vanishing solution. Since q is computed by the results of the diffusion equation in the RM, the degree l can only assume the values 0 and 1, with the second moment φ_1 equal to the net current J. Therefore, the sum over l will always be truncated in the following.

Multiplication of Equation (4) by μ and the integration over $[-1,1]$ provides the expression for the current, see (Tomatis and Dall'Osso 2011). The integration on μ yields integral exponential functions by a simple change of variable ($\mu = \pm 1/u$, according to the sign of μ) (Abramowitz and Stegun 1964):

[1]Curly bracket remind the possible use of the k-eigenvalue in case of vanishing external sources.

$$E_n(\tau) = \int_0^1 d\mu \; e^{-\tau/\mu}\mu^{n-2} = \int_1^\infty du \; e^{-\tau u}u^{-n}, \;\; n \geq 0.$$

These special functions are then used to compute the current at the cell interfaces for all i:

$$\begin{aligned} J_{g,i+1/2} = &\int_0^1 d\mu \; \mu\varphi_g(a,\mu)e^{-\tau_g(a,x_{i+1/2})/\mu} - \int_0^{-1} d\mu \; \mu\varphi_g(b,\mu)e^{-\tau_g(b,x_{i+1/2})/\mu} \\ &+ \sum_{j=0}^{I-1}\left[\mathrm{sgn}(x_{i+1/2}-x_{j+1/2})\frac{q_{0,g,j}}{2}\int_{x_{j-1/2}}^{x_{j+1/2}} dx' E_2\left(\left|\tau_g(x',x_{i+1/2})\right|\right)\right. \\ &\left. + \frac{3}{2}q_{1,g,j}\int_{x_{j-1/2}}^{x_{j+1/2}} dx' E_3\left(\left|\tau_g(x',x_{i+1/2})\right|\right)\right] \end{aligned} \quad , \tag{6}$$

where $q_{(\cdot),g,j}$ are the moments of the source q_g from Equation (5) averaged in the volume of the jth cell:

$$q_{0,g,j} = \sum_{g'}(\sigma_{s,0,g'\to g,j} + \chi_g \nu\sigma_{f,g',j})\phi_{g',j}, \tag{7a}$$

$$q_{1,g,j} = \sum_{g'}\sigma_{s,1,g'\to g,j}J_{g',j}. \tag{7b}$$

The current appearing in $q_{1,g,j}$, that is in case of linearly anisotropic scattering, is also to be considered as volume-averaged in the cell j. The optical lengths τ in Equation (6) show the subscript g because they are evaluated with the corresponding total cross section $\sigma_{t,g}$. For the property $E'_{n+1}(\ell) = -E_n(\ell)$, the spatial integrals of the integral exponential functions can be solved analytically by integrating on τ:

$$\begin{aligned} &\int_{x_{j-1/2}}^{x_{j+1/2}} dx' E_n\left(\left|\tau_g(x',x_{i+1/2})\right|\right) = \frac{\mathrm{sgn}(x_{i+1/2}-x_{j+1/2})}{\sigma_{t,g,j}} \\ &\cdot\left[E_{n+1}\left(\left|\tau_g(x_{j+1/2},x_{i+1/2})\right|\right) - E_{n+1}\left(\left|\tau_g(x_{j-1/2},x_{i+1/2})\right|\right)\right]. \end{aligned}$$

These quantities can be computed for $i > j$ only, because the others are simply opposite in sign (anti-symmetric). Equation (6) can be reformulated for the partial currents, thus considering only the contributions coming from the different sides of $x_{i+1/2}$. Omitting the index on groups and keeping only isotropic sources, this is:

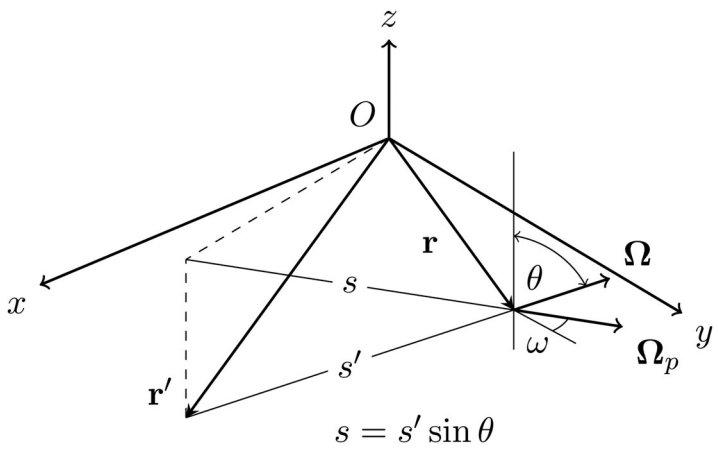

Figure 2. Projection of vectors on the *x*-*y* plane.

$$J^{\pm}_{i+1/2} = \sum_{j=1}^{I} q_{0,j}\Delta_i \tilde{e}^{\pm}_{i+1/2,j} + J^{\pm}(x_b)\tilde{t}_{i+1/2,x_b}. \tag{8}$$

We make explicit use of the theory of the collision probability method (CPM; Lewis and Miller 1984; Hébert 2009) to write Equation (8). $\tilde{e}_{i+1/2,j}$ represents the probability of a neutron emitted isotropically in Δ_i to escape uncollided at $x_{i+1/2}$, along its positive or negative direction of flight. The expression for $\tilde{e}$ can be derived straightforwardly from Equation (6) by rearranging the terms in the sum at the right-hand side. $\tilde{t}_{i+1/2,x_b}$ is the transmission probability of a neutron to enter isotropically at x_b and to cross the interface at $x_{i+1/2}$ without colliding hitherto, i.e. $\tilde{t}_{i+1/2,x_b} = 2E_3(\tau(x_{i+1/2}, x_b))$. A discussion about the transmission probability follows in Section 4.

3.2. Cylindrical geometry

The expression of the current in curvilinear geometries is derived in this section from the 3D Cartesian geometry, where the angular flux at point $\mathbf{r}$ along the direction of flight $\mathbf{\Omega}$ is given by the general expression (Lewis and Miller 1984):

$$\begin{aligned}\varphi(\mathbf{r},\mathbf{\Omega}) = &\int_0^{S'} ds'\ q(\mathbf{r} - s'\mathbf{\Omega},\mathbf{\Omega}) \exp\left(-\tau(\mathbf{r},\mathbf{r} - s'\mathbf{\Omega})\right) \\ &+ \varphi(\mathbf{r} - S'\mathbf{\Omega},\mathbf{\Omega}) \exp\left(-\tau(\mathbf{r},\mathbf{r} - S'\mathbf{\Omega})\right),\end{aligned} \tag{9}$$

that is considering the contribution of the source q within the distance $S'(\mathbf{r},\mathbf{\Omega})$ from the boundary and the possible entering amount of particles therein. All contributions are collected at $\mathbf{r}$ by exponential attenuation

along the traveled optical path, that is according to the probability of still continuing the first flight after emission. We examine first the case of the cylinder as a particular case of the 2D frame. In planar geometry, the angular flux and the source do not depend on the axial coordinate z. Hence, the position on the characteristic line identified by $\mathbf{\Omega}$ is projected on the x-y plane (see Figure 2): $\varphi(\mathbf{r}-s'\mathbf{\Omega},\mathbf{\Omega})=\varphi(\mathbf{r}-s\mathbf{\Omega}_p,\mathbf{\Omega})$ and likewise for q, with the unit vector $\mathbf{\Omega}_p$ lying on the x-y plane. θ is the polar angle measured between $\hat{e}_z$ and $\mathbf{\Omega}$. In absence of incoming particles, this allows to rewrite Equation (9) as:

$$\varphi(\mathbf{r},\mathbf{\Omega})=\int_0^S ds\ \frac{q(\mathbf{r}-s\mathbf{\Omega}_p,\mathbf{\Omega})}{\sin\theta}\exp\left[-\frac{\tau(\mathbf{r},\mathbf{r}-s\mathbf{\Omega}_p)}{\sin\theta}\right]. \tag{10}$$

As well, integration of Equation (10) over the solid angle $d\mathbf{\Omega}=\sin\theta d\omega d\theta$ yields the scalar flux at point $\mathbf{r}$. The theory of CPMs originates from the use of flat isotropic sources in the cells of the spatial mesh. The use of anisotropic sources with spatial variation in the same cells, for instance polynomial-like, is possible but leads to much more difficult expressions to solve. Two integrations in space arise for each direction $\mathbf{\Omega}$, connecting the source in region j to the flux (or its total reaction rate) in region i by means of its collision probability. The incoming flux is usually considered as isotropic too, or linearly anisotropic in angle as in (Hébert 2009) to relate the partial entering and outgoing currents to the only first flux moments. These partial currents on the boundary must satisfy a general condition of albedo.

Using standard nomenclature of CPMs, transfer probabilities refer to particles entering the problem domain and leaving it without incurring into any collision. They can provide the probability of reflection in case the entering and the leaving surfaces are the same. The probability of escape deals with neutrons produced in a given region and leaving a surface, still uncollided. These probabilities are employed to write the integral transport equations for the volume-averaged scalar flux (or its total reaction rate) in each cell, and the surface-averaged currents at the cell interfaces.

The projections of partial currents on the outward normal $\hat{n}$ to a given surface are obtained from integration of Equation (10) in $d\mathbf{\Omega}$ with the weight $|\hat{n}\cdot\mathbf{\Omega}|=\sin\theta|\hat{n}\cdot\mathbf{\Omega}_p|$ on $\hat{n}\cdot\mathbf{\Omega}\lessgtr 0$. Higher moments can be obtained by the weights associated to the corresponding spherical harmonics. Integration along the polar angle is resolved analytically by the Bickley-Naylor functions (Amos 1983):

$$\mathrm{Ki}_n(\tau)=\int_0^{\pi/2} d\theta\sin^{n-1}\theta\exp\left(-\frac{\tau}{\sin\theta}\right),\ \ n\geq 0. \tag{11}$$

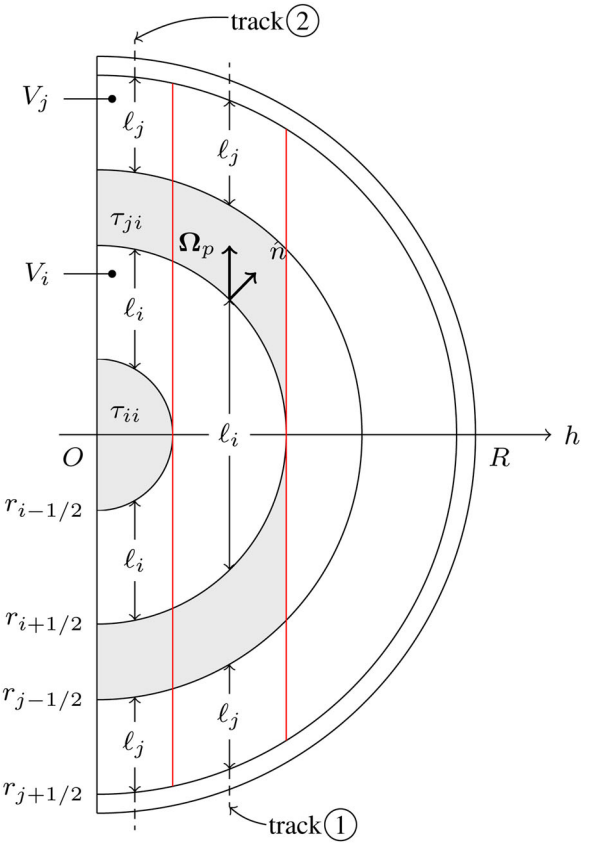

Figure 4. Integration along the tracks in the 1D cylindrical geometry (suggested by Fig. 3.17 of reference (Hébert, 2009)).

The properties used for the computation of these functions are available elsewhere (Lewis and Miller 1984; Hébert 2009). We use the Fortran library by Amos from 1983 in this work (Amos 1983).

After introducing these arguments for a bare cylinder, the current leaving the cylindrical surface at $\mathbf{r}$ (with direction $\hat{n}$) given by neutrons flying along $\mathbf{\Omega}_p$ is:

$$J^+(\mathbf{r}) = \frac{1}{2\pi}\int_{W^+} d\omega \ \left|\hat{n}\cdot\mathbf{\Omega}_p\right| \int_0^S ds \ \mathrm{Ki}_2\left[\tau\left(\mathbf{r}, \mathbf{r}-s\mathbf{\Omega}_p\right)\right] q(\mathbf{r}-s\mathbf{\Omega}_p), \tag{12a}$$

with $W^+ = \left\{\omega | \hat{n}\cdot\mathbf{\Omega}_p > 0\right\}$. Using the surface element $dA' = sd\omega ds$ and $\mathbf{r}'_p = \mathbf{r} - s\mathbf{\Omega}_p$, it is also:

$$J^+(\mathbf{r}) = \int_{W^+\times[0,S]} dA' \ \hat{n}\cdot(\mathbf{r}-\mathbf{r}'_p) \ \frac{\mathrm{Ki}_2\left[\tau\left(\mathbf{r},\mathbf{r}'_p\right)\right]}{2\pi\left|\mathbf{r}-\mathbf{r}'_p\right|^2} q(\mathbf{r}'_p). \tag{12b}$$

J^- is obtained with integration over $w \in W^- = \left\{\omega | \hat{n}\cdot\mathbf{\Omega}_p < 0\right\}$ instead.

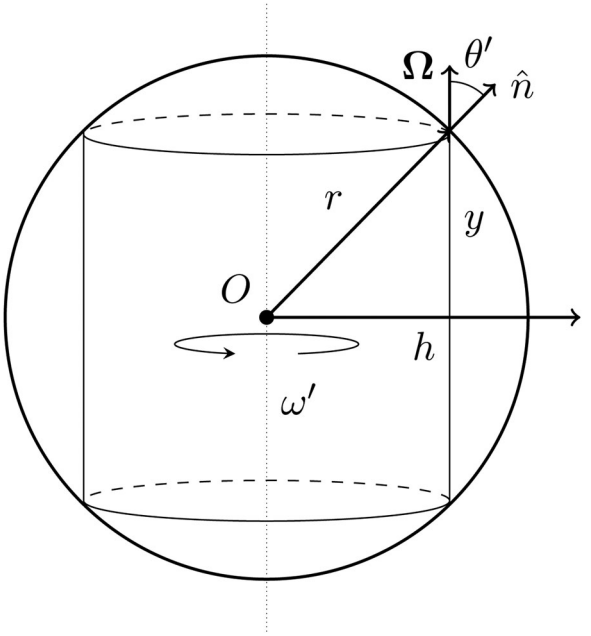

Figure 3. Use of symmetry in the sphere for integration over the surface.

Another integration on the total surface $S(r) = \int r d\theta' = 2\pi r$, with $\theta' = \hat{n} \cdot \mathbf{\Omega}_p$, is necessary to obtain the current density in the 1D frame. For a given angle ω, we have then volume integrals to solve numerically along many parallel lines called tracks, see Figure 4, for $r d\theta' = dh/\cos\theta'$. Furthermore, the tracks are identical for any angle ω in the 1D cylindrical geometry factoring out 2π from the integrals in Equations (12), which can also be limited to half portion of the cylinder thanks to its symmetry. Finally, the outgoing and incoming currents at r become:

$$J^{\pm}(r) = \pm \frac{1}{\pi r} \int_0^r dh \int_{-Y}^{\pm y} d\ell \ \mathrm{Ki}_2\big[\tau(y, y-\ell)\big] q(h, y-\ell) \tag{13}$$

with $y(r,h) = \sqrt{r^2 - h^2}$, $Y = y(R,h)$ and the outer radius R. After multiplication by $S(r)$ and still with uniform sources, Equation (13) can be written in terms of the escape probability $\tilde{e}_j(r)$ for a neutron to be emitted isotropically in ring j and to leave uncollided along the normal direction the semi-cylinder surface at r, being crossed with angle $\omega \in W^{\pm}$:

$$\begin{aligned} J^{\pm}(r) S(r) &= \sum_j q_j V_j \left[\pm \tilde{e}_j^{\pm}(r)\right] \ \text{with} \ \tilde{e}_j^{\pm}(r) \\ &= \frac{2}{V_j} \int_0^r dh \int_{L_j^{\pm}} d\ell \ \mathrm{Ki}_2\big[\tau(y, y-\ell)\big], \end{aligned} \tag{14}$$

$L_j^{\pm}(h) = [-Y, \pm y] \cap V_j$ and where V_j is the ring area. $\mathrm{Ki}_2\big[\tau(y, y-\ell)\big]$ is the

transport kernel expressing the probability of a neutron to travel uncollided along ω for a length τ, given in mean free path units, from $(y-\ell)$ to y (Stamm'ler and Abbate 1983). The integral on the track ℓ is written differently for the convex and for the concave parts of the rings with respect to the direction of flight, see for instance track 1 and 2 in Figure 4 where the same notation of Figure 1 is used for the radial mesh. The current leaving the ith ring at $r_{i+1/2}$ gets all source contributions weighted with the quantities $\varepsilon^{+}_{i+1/2,j} = V_j \tilde{e}^{+}_{i+1/2,j}$:

$$\varepsilon^{+}_{i+1/2,j} = 2 \cdot \begin{cases} \int_0^{r_{i-1/2}} dh \int_0^{\ell_j} d\ell \Big[\\ \qquad \mathrm{Ki}_2\big(2\sigma_i\ell_i + \tau_{ii} + \tau_{ij} + \sigma_j\ell\big) \ \text{ if } \ i<j \\ \quad + \mathrm{Ki}_2\big(\sigma_i\ell_i + (1-\delta_{ij})(\tau_{ij}+\sigma_j\ell_j) + \tau_{jj} + \sigma_j\ell\big) \ \text{ if } \ i\geq j \\ \quad + \mathrm{Ki}_2\big((1-\delta_{ij})(\sigma_i\ell_i+\tau_{ij}) + \sigma_j\ell\big) \ \text{ if } \ i\geq j \\ \Big] + \int_{r_{i-1/2}}^{r_{i+1/2}} dh \ y \int_0^{\ell_j} d\ell \ \mathrm{Ki}_2\big((1-\delta_{ij})(\sigma_i\ell_i+\tau_{ij}) + \sigma_j\ell\big) \ \text{ if } \ i\leq j, \end{cases} \tag{15}$$

using the Kronecker function $\delta_{ij} = 1$ only if $i=j$ and null otherwise. τ_{ij} and τ_{ii} are respectively the optical lengths between the rings i and j, and across the outer diameter of ring i. The radial integral includes all rings within $r_{i+1/2}$. The integrals involving the Ki function are solved thanks to the property $d_\tau \mathrm{Ki}_n(\tau) = -\mathrm{Ki}_{n-1}(\tau)$.

The corresponding form for the reduced escape probability for the incoming current is

$$\varepsilon^{-}_{i+1/2,j} = 2 \int_0^{r_{i+1/2}} dh \int_0^{\ell_j} d\ell \ \mathrm{Ki}_2\big(\tau_{ji} + \sigma_j\ell\big), \tag{16}$$

for $i<j$, whereas $\varepsilon^{-}_{i+1/2,j} \equiv 0$ for $i \geq j$ since in this case a neutron born in volume j (or in volume $j=i$) cannot enter volume i through its outer surface at radius $r_{i+1/2}$ without undergoing a collision. The useful reciprocity and conservation properties commonly used in CPM solvers to save the total computational effort can be applied only after calculating the first flight collision probabilities.

Singularity of the integrand for the h-integration introduced in Equation (13) is known in the convex part while computing the collision probabilities (Hébert 2009; Stamm'ler and Abbate 1983); this notably happens at the outer radius of the jth ring where $\hat{n}$ is perpendicular to $\mathbf{\Omega}_p$. However, that integral can be regularized by a suitable change of variable, see Appendix A. The calculation of the escape probabilities as presented in this section is also affected by this endpoint singularity. Because of this

singularity, the integral in h can then be resolved numerically with weights and points by the Gauss-Jacobi quadrature, which is one order more accurate than the common Gauss-Legendre quadrature.

3.3. Spherical geometry

The derivation of the scalar flux and of the current in the sphere follows the same rational adopted in Section 3.2 by angular integration of Equation (9) and exploiting the symmetries available in the given coordinate frame. Because of the rotational symmetry, any direction of flight lays on a spherical cut passing through the origin ($\mathbf{\Omega}_p = \mathbf{\Omega}$), see Figure 3. The integration to carry for each direction $\mathbf{\Omega}$ over the spherical surface $S(r) = \int r^2 \sin\theta' d\theta' d\omega' = 4\pi r^2$ shows a case similar to the cylinder of Figure 4, with integration on the semicircle along the coordinate h, thanks to the axial symmetry around ω' that factors out 2π, but with the new weight $h = r\sin\theta'$. The tracking integrals up to the spherical surface are the same for all directions, so that the integration over the unit solid angle yields simply 4π, canceling out the probability of isotropic emission used for the source. Figure 3 is specific to the calculation of the positive radial partial currents. Negative partial currents need taking into account the sources outside the depicted sphere of integration.

Using the same quantities defined in Equation (13), Equation (14) holds also for the sphere but using the new reduced escape probability:

$$\varepsilon_j(r) = 2\pi \int_0^r dh\ h \int_{L_j} d\ell\ \exp\left[-\tau(y, y-\ell)\right]. \tag{17}$$

Endpoint singularities at integration stand also in this case. The derivation of the equation for the current leaving the ith spherical surface can be obtained straightforwardly from Equation (15).

3.4. Derivation of collision probabilities

The probabilities used to solve the integral transport equation can treat a volume or surface source, and similarly for the target quantity after emission. Indeed, they consider only the first flight of particles until collision in the target or leakage from its boundary (being still uncollided). The first flight collision probability is then the probability that a neutron emitted isotropically in a cell volume suffers its first collision in another or within itself. This is equivalent to count the number of first collisions in the same target volume produced by a unitary source in the starting volume. This number cannot be an integer of course.

After all escape and inscape probabilities are known, the first flight collision probabilities can be determined by conservation properties in order to

reduce the amount of total operations. The escape probabilities obtained from Equations (15) and (16) yield the number of neutrons leaving a surface uncollided. For instance, the probability $\tilde{p}$ for a neutron emitted isotropically in the region i to collide in the same region must fulfill the following relation:

$$\tilde{p}_{ii} + \tilde{e}^{+}_{i+1/2,\,i} + \tilde{e}^{-}_{i-1/2,\,i} = 1, \quad \forall i. \tag{18a}$$

$\tilde{e}$ denotes a total escape probability introduced above. This can be generalized with neutrons coming from region j and colliding in region i as:

$$\tilde{p}_{ij} = \tilde{e}^{+}_{i-1/2,\,j} - \tilde{e}^{+}_{i+1/2,\,j} + \tilde{e}^{-}_{i+1/2,\,j} - \tilde{e}^{-}_{i-1/2,\,j} + \delta_{ij}, \tag{18b}$$

with $\tilde{e}^{\pm}_{\mp 1/2,\,j} = 0, \ \forall j$ in the sphere and in the cylinder. A formulation resolving the integral Boltzmann equation by first-flight escape probabilities was already introduced by Bitelli and Turrin (1974, 1976).

Particle conservation on the full domain requires $\sum_i \tilde{p}_{ij} + \tilde{e}^{+}_{I+1/2,\,j} = 1$, $\forall j$. At last, reciprocity implies

$$\frac{\tilde{p}_{ij}}{V_i \sigma_i} = \frac{\tilde{p}_{ji}}{V_j \sigma_j} \quad \text{and} \tag{19a}$$

$$\frac{\tilde{p}_{j,\,i+1/2}}{V_j \sigma_j} = 4 \frac{\tilde{e}^{+}_{i+1/2,\,j} + \tilde{e}^{-}_{i+1/2,\,j}}{S_{i+1/2}}, \tag{19b}$$

for $1 \leq i, j, \leq I$. Equation (19a) can also be used to verify the implementation of the escape probabilities. Collision probabilities with surface source emission from Equation (19b) are needed with non-zero entering currents of neutrons at the boundary $x_{I+1/2}$. This probability refers again to an angular flux entering the surface $(i + 1/2)$ isotropically, yielding the cosine current typical of white reflection.

Transmission probabilities between surfaces are also needed in response matrix formulations and with boundary conditions different from vacuum. The response matrix formulation partitions the calculation domain in separate blocks, which exchange out-going and entering partial currents to update their internal distributions of reaction rates. The method to solve the integral transport equation by the CPM providing reference solutions for the RM is reported in Appendix B.

It might not be possible to compute the escape probabilities as derived in this work using existing computer codes that employ the CPM without code modifications. In fact, existing codes usually calculate directly the collision probabilities, by which all other probabilities are determined next using reciprocity and conservation properties. Besides, these codes only need to calculate the escape probability from the outer boundary surface.

4. Boundary conditions

A generalized form for the boundary condition of the diffusion equation applying at the left side of the slab follows as $\Upsilon = -D_0\phi_0/(\Delta_0/2+\zeta)$, where ζ is the extrapolation length in case of vacuum. $\zeta = 2D$ yields the Marshak boundary conditions for instance, but the value $\zeta = 2.13D$ is usually recommended in slab geometry (Stamm'ler and Abbate 1983). Reflection can be reproduced by $\zeta \to \infty$, whereas the condition of zero-flux comes with $\zeta = 0$. The boundary δJ takes the simpler form $\delta J = -\delta D_{-1/2}\phi_0$ without dividing by the spatial width, since no particular extrapolation length is meant for the correction. Indeed, it will be possible to determine the actual extrapolation length only at convergence. The expression for the right boundary is straightforward, implying a non-negative current. Reflection is always assumed at the center in curvilinear geometries.

About the currents from Equation (6), the boundary conditions must be implemented through the first two terms at the right side due to the incoming flux. They are zero by definition only in case of vacuum. The flux expansion on the Legendre polynomials is necessary to reproduce other types of boundary condition. Again, we can only approximate the flux up to the first order, that is $\varphi \approx \phi/2 + 3/2J\mu$. This approximation may not reproduce a vanishing current with reflection reproducing a symmetric distribution. Only situations with perfectly isotropic angular flux at the boundary will be described correctly. At the left boundary for instance, the current can be expressed as $J(a) = J^+ + J^- = 0$ with the entering current $J^+ = \int_0^1 d\mu\mu\varphi(a,\mu) = -J^-$. J^- takes into account all contributions coming from the right of a up to b, see Equation (6). In the absence of higher moments, the angular flux at the boundary becomes simply $\phi(a,\mu) \approx \varphi_0(a)/2$, yielding $J^+(x) = E_3(\tau(a,x))\varphi_0(a)/2$, or $J^+(x) = \tilde{t}_a(x)\phi(a)/4$ using the CPM formalism (white reflection at a). Here, $\tilde{t}$ is the transmission probability of neutrons crossing uniformly and isotropically the surface a to get to the position x uncollided. The value of this probability can be obtained through reciprocity and conservation properties, as shown in Section 3.4. Hence, this approximation does not guarantee to obtain the expected vanishing current at the boundary when computing the same current at the boundary with symmetric flux distributions. However, it is possible to determine the difference between the partial currents (remind that J^- is negative). The higher (even) flux moments are responsible for this residual quantity, but they are not available unfortunately. A possible solution is considering that this quantity comes artificially from the only second moment, like[2]

[2]The operator $+=$ assigns to J the sum of itself and quantity to the right.

Table 1. One-group cross section values used in the benchmark problems.

Material	ν	σ_f	σ_c	σ_s	σ_t	c
Pu-239 (PUa)	3.24	0.081600	0.019584	0.225216	0.32640	1.50
Pu-239 (PUb)	2.84	0.081600	0.019584	0.225216	0.32640	1.40

$$J^+(x)+ = \frac{5}{4}\tilde{\varphi}_2(a)[3E_5(\tau(a,x)) - E_3(\tau(a,x))],$$
$$\text{with } \tilde{\varphi}_2(a) = -\frac{16}{5}\left(\frac{1}{4}\varphi_0(a) + J^-\right). \tag{20}$$

The flux expansion at the left boundary is then

$$\phi(a,\mu) = \frac{1}{2}\varphi_0 + \frac{3}{2}\mu\varphi_1 + \frac{5}{4}\left(3\mu^2 - 1\right)\tilde{\varphi}_2,$$

with $\varphi_1 = J = 0$ with reflection. The derivation of the correction at the other boundary of the slab can easily be derived.

Transmission probabilities of neutrons entering with anisotropic (even) distributions are now needed, but this time they cannot be derived from the escape probabilities based on isotropic emission. We only give the expression to calculate these quantities in the slab, since white reflection is generally preferred in the 1D curvilinear geometries for reproducing more accurate physical results.

Although this correction definitely improves the results, it cannot yield exactly the same results of the unfolded geometry, that is without reproducing the half symmetry by reflection. This occurs because the small current difference is allotted only to the second moment, neglecting the others which may become relevant on a case-dependent basis.

5. Results

New computer programs have been developed in Python v3.8.2 with the numerical libraries NumPy v1.18.2 and SciPy v1.3.2 in order to solve the diffusion and the transport problems after calculating the first flight escape probabilities in the three geometries. The programs can treat heterogeneous media and use the multigroup formalism in energy, being intended mainly for educational purposes.

We present in this section one-group homogeneous critical problems with isotropic scattering to study the behavior of the RM with angular redistribution in the curvilinear geometries. These cases belong to a test set of analytical benchmarks for code verification (Sood, Forster, and Kent Parsons 2003). The setup of the complete test suite with problems of increasing level of complexity is planned as future research action. Although analytical solutions exist in the literature, reference solutions are

Table 2. Reference critical lengths r_c of the test cases, with the multiplication factor k_D and the geometrical buckling B_G^2 of the analytical solution in diffusion.

		r_c			
Problem Id.	Geometry type	(mfp)	(cm)	k_D	B_G^2
PUa-I-0-SL	Slab	0.605055	1.853722	0.891973	0.191159
PUb-1-0-SL	Slab	0.736603	2.256751	0.913739	0.149267
PUb-1-0-CY	Cylinder	1.396979	4.279960	0.956090	0.138266
PUb-1-0-SP	Sphere	1.985343	6.082547	0.964129	0.136287

Table 3. Analytical solutions from diffusion in centered, bare, and homogeneous one-group problems of length X (vacuum boundary with extrapolation distance $d = \zeta D$).

Geometry type	Solution	B_G, s.t.
Slab	$\cos(B_G x)$	$\tan(B_G X) = 1/(dB_G),\ B_G \in (0, \pi/(2X))$
Cylinder	$J_0(B_G x)$	$J_0(B_G X) - dB_G J_1(B_G X),\ B_G \in (0, 2.404825/X)$
Sphere	$\sin(B_G x)/x$	$B_G X - (1 - X/d)\tan(B_G X),\ B_G \in (\pi/(2X), \pi/X)$

here provided by the CPM, whose implementation takes advantage of the escape probabilities derived in Section 3, and whose numerical solution is explained in Appendix B. Besides, reference values of the fundamental flux are provided by the benchmark problems at a few positions.

The problems are resolved in units of optical length according to the change of variable $x \leftarrow \sigma x$. The isotropically multiplying source becomes $q = c\varphi_0/4\pi$ with the number of secondaries from scattering and fission events $c = (\sigma_s + \nu\sigma_f)/\sigma$. The transport equation to solve is then:

$$\left(\mu \frac{\partial}{\partial x} + 1\right)\varphi(x, \mu) = \frac{c}{4\pi}\int_{-1}^{1} \varphi(x, \mu) d\mu$$

The multiplicity ν recovers the role of eigenvalue in absence of external sources. The size of the problem is simply $b = r_c$ with $a = 0$. The material specifications of the benchmark cases are reported in Table 1. The naming convention of the test cases follows Sood et al., with the critical lengths listed in Table 2. All problems use the vacuum boundary condition.

The analytical solutions from diffusion theory are available in Table 3, where the geometrical buckling B_G^2 is given by the root of the transcendental equations in the last column. The multiplication factor k_D of the analytical diffusion problem is obtained by equating the geometrical buckling and the material buckling $B_M^2 = (\nu\sigma_f/k - \sigma_a)/D = (k_\infty/k - 1)/L^2$, where $k_\infty = \nu\sigma_f/\sigma_a$ is the multiplication factor in the infinite medium and $L^2 = D/\sigma_a$ is the diffusion area. The benchmark problems provide the reference transport fundamental flux at given positions, see Table 4. The scalar fluxes are all normalized to be unitary at the center.

After computing the numerical solution of the diffusion problem by finite differences without corrections at the cell interfaces, we evaluate new current estimates by using escape, transmission, and reflection probabilities

Table 4. Fundamental flux from the reference transport solution of the benchmark.

		$r = x/r_c$			
Problem Id.	Geometry type	$r_1 = 0.25$	$r_2 = 0.5$	$r_3 = 0.75$	$r_4 = 1$
PUb-1-0-SL	Slab	0.970173	0.881054	0.731813	0.490259
PUb-1-0-CY	Cylinder	–	0.8093	–	0.2926
PUb-1-0-SP	Sphere	0.935380	0.755753	0.498843	0.192226

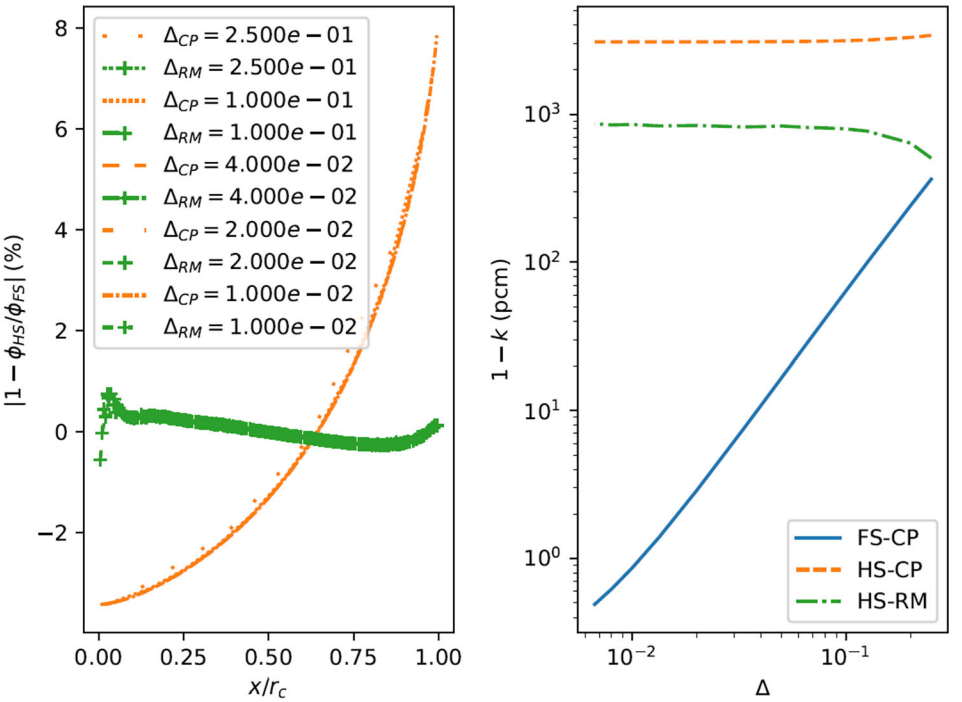

Figure 5. Error in the half slab (PUa-1-0-SL) with white reflection at the right and vacuum at the left; HS and FS indicate half slab and full slab, respectively.

according to the given geometry type, as derived from the integral equation in Section 3. Then, the solution by the RM is sought iteratively as explained in Section 2. Four integration points are used in the Gauss-Jacobi quadrature, yielding an error lower than 0.1%. The solution by diffusion in these particular test cases is very different from the one by transport, which provides the physical solution. Anderson acceleration through the DAAREM algorithm (Damped Anderson Acceleration with Epsilon Monotonicity) is also used during the iteration process (Henderson and Varadhan 2019), reducing considerably the number of iterations to achieve residuals on the relative flux differences below 10^{-6}. Its use is crucial to find the fixed point solution throughout the non-linear iterations of the RM. Very low convergence rates have been noticed without DAAREM, potentially leading to

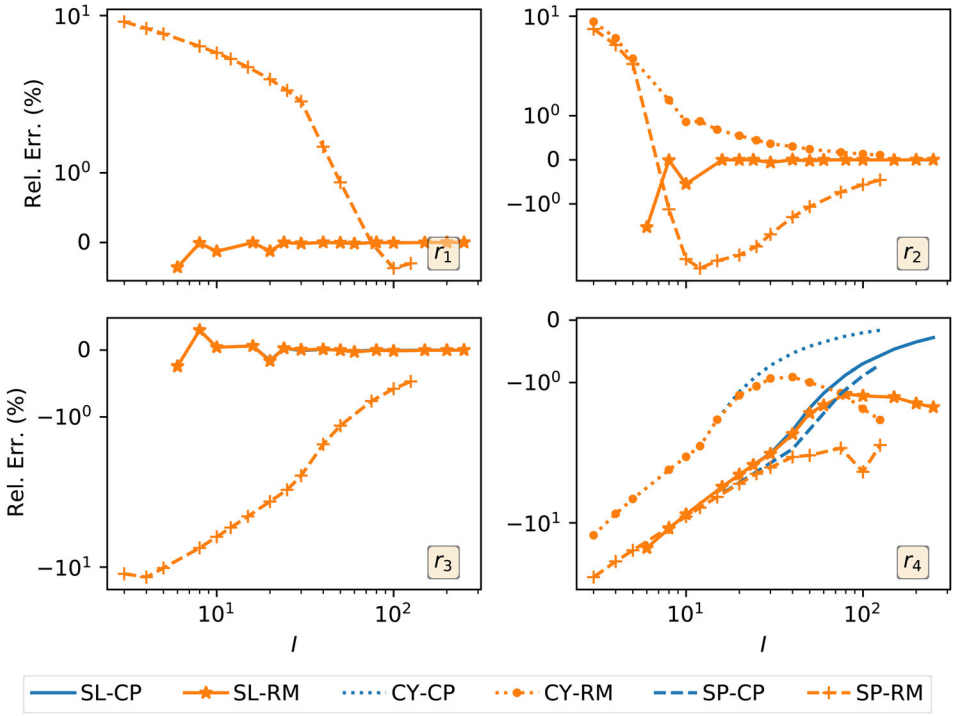

Figure 6. Relative error in percent of the fundamental flux for all PUb cases.

detect false convergence after a very high number of iterations, which means obtaining the wrong flux solution afterwards.

The calculation of half slab by CPM after setting (white) reflection at the center yields poor results due to missing contributions from the higher flux moments, see Figure 5. Equidistant meshes are used by refining gradually the cell width Δ. The solution obtained by RM takes into account the artificial correction applied to the only second moment, reducing the flux error (see the green curves in the left plot), but its eigenvalue solution is higher than 1 of 836 pcm on converged meshes. The eigenvalue computed by CPM on half slab is lower than 1 of about 3000 pcm (see the right plot). This issue, discussed in Section 4, is more severe with very thin slab, like in the case PUa-1-0-SL, and disappears when the slab thickness r_c increases beyond a few mean free paths (mfp). This forces the modeling of the full slab when verifying the flux distribution for the case PUb-1-0-SL. Such issue does not appear at the center of the solid cylinder or sphere. All methods computes a critical configuration for PUa-1-0-SL after unfolding the half-slab. The study to verify the fundamental flux is then shown only for the case PUb-1-0-SL.

About the cases PUb, the relative error on the critical flux computed by CPM against the values from Table 4 are shown in Figure 6 for increasing number of cells (I) with equivolume meshes. The same figure shows also

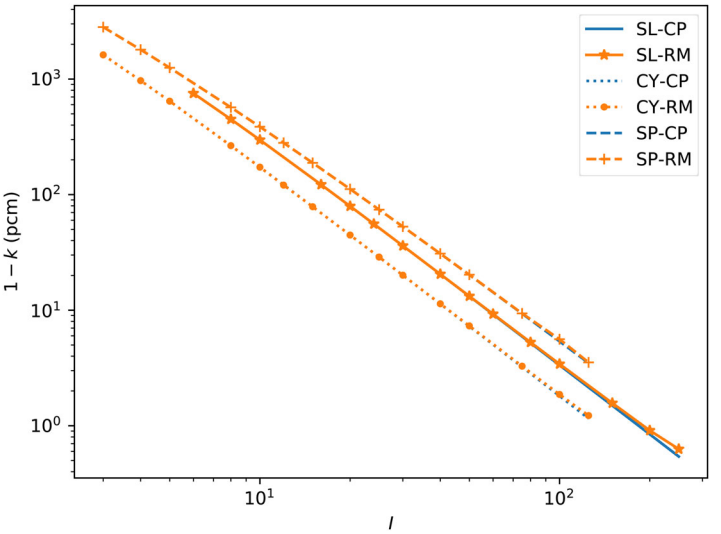

Figure 7. Error in pcm of the multiplication factor k in the PUb critical benchmark problems.

the results obtained by RM. Basically, RM and CPM results overlap but at the vacuum boundary where the monotonic behavior of the error trend is broken with fine meshes, leaving a residual error of about 1–2% in the slab and in the cylinder, and higher than 3% in the sphere. The spherical geometry needs finer meshes to decrease the error, which is still higher near the outer boundary. Refined meshes near the boundary, drawn for instance by a geometric progression with ratio less than one, can lower this error, see the program released with this publication. The flux at the boundary used to reproduce the current by diffusion is approximated by a quadratic polynomial fitting the midpoint fluxes at the nearest three cells, instead of the only flux of the last cell.

The deviation of the multiplication factor from unity by refining the mesh is shown in Figure 7. When unfolding the reflected slab, the number of cells in the slab is doubled indeed for taking a thickness of $2r_c$ in the calculations. This explains why the plotted error for the slab is higher than the one for the cylinder at a given value of I. The same trend for the three geometries is noticed, with the spherical one needing finer meshes to achieve the same level of error. The multiplication factor computed by RM is about the same as the one given by CPM.

The solution by CPM needs a single inversion of a full matrix with the direct and fast solving scheme reported in Appendix B. This scheme may not be suitable to problems with a high number of energy groups and spatial cells. The RM needs to invert several times a tridiagonal matrix, which is efficiently performed in our code by the Thomas TDMA algorithm, a simplified form of Gaussian elimination that can be used to solve tridiagonal systems of equations (Quarteroni, Sacco, and Saleri 2007). Both

methods share the calculation part of the first flight escape and collision probabilities. Typical runtimes of the benchmark problems treated in this article are quite fast (a few seconds or minutes depending on the size of the problem), and they can be easily run on any laptop computer. The calculation of the first flight probabilities is the most expensive part, especially in curvilinear geometries, and it should be reprogrammed in a compiled language to save runtime.

6. Conclusion

Initially the RM was proposed for better estimates of the diffusion coefficient by calculating the current with a higher-order transport operator and a known best-estimate neutron flux (Ronen 2004). This can originate an iterative scheme leading to new flux distributions solved by a diffusion solver yet with the aim to fulfill the integral transport equation. The direct resolution of the integral equation, as in the CPM, implies the inversion of full matrices, with generally poor control of their conditioning. The solution of the diffusion equation offers many numerical advantages instead, solution speed and robustness above all.

Furthermore, the same current obtained by the higher-order operator can be enforced in the discretized form of the diffusion equation as suggested by the CMFD scheme, which avoids the numerical issues arising with flat flux. This is also the option adopted in this work. In particular, the RM is here developed under the common formalism of CPM theory, thus offering a formal derivation in the framework of integral transport with the nonlinear iterations of the CMFD scheme. Only first flight escape probabilities are computed, by which all other kinds of probabilities are derived using conservation and reciprocity properties.

The implementation of the boundary conditions is improved to reproduce the expected vanishing current in case of reflection. However, this correction is not sufficient to remove the limitations due to the use of white reflection, which is particularly serious in problems smaller than a mean free path.

The solutions are verified with simple one-group homogeneous problems and isotropic sources from the benchmark test suite by Sood, Forster, and Kent Parsons (2003). More benchmark problems will be analyzed in a future work to study the RM with material heterogeneity and with many energy groups. The application of the RM to problems with anisotropic scattering suffers from the lack of the flux moments higher than the first since diffusion can count only on the scalar flux and on the net current. This article shows the extension of the RM to linearly anisotropic scattering in the source terms in the case of the slab. The study of anisotropy still needs further developments.

The use of Anderson acceleration implemented in the RM iterations with the DAAREM algorithm was crucial to find converged results, fixing the issue of slow convergence noticed in the previous published works (Tomatis and Dall'Osso 2011; Gross, Tomatis, and Gilad 2020). The large discrepancy on the scalar flux observed in previous works at bare vacuum boundaries has now been reduced to a few percent with respect to the reference solutions. However, it is still necessary to investigate these remaining differences at the boundary, like using for instance higher-order numerical approximations of the discretized equations. This strong improvement in the flux behavior suggests that the same test problems could have been affected in the past implementations by false convergence for very slowly decreasing convergence rates. Additional tests are on-going to verify this assertion. The upgrade of the RM to coarser meshes and different implementations of the CMFD scheme will be the objects of future research and development. These are considered as central topics for the advancement of the methodology in practical applications.

Additional material

The theory and results of this article were produced by the computer program available at https://github.com/ndarmage/RM1D.git. This program is freely distributed for educational purposes and basic training in transport theory, without containing any confidential material on nuclear data.

Acknowledgments

The authors express their gratitude to Prof. Yigal Ronen who initiated the method.

ORCID

Daniele Tomatis http://orcid.org/0000-0001-7314-2227

References

Abramowitz, M., and I. A. Stegun. 1964. *Handbook of mathematical functions with formulas, graphs, and mathematical tables*. New York: Dover Publications.

Amos, D. E. 1983. Algorithm 609: A portable FORTRAN subroutine for the Bickley functions $\mathrm{Ki}_n(x)$. *ACM Trans. Math. Softw.* 9 (4):480–93. doi:10.1145/356056.356064

Amos, D. E. 1983. Uniform asymptotic expansions for exponential integrals e_ n (x) and bickley functions ki n (x). *ACM Trans. Math. Softw.* 9 (4):467–79.

Bitelli, G., and A. Turrin. 1974. Evaluation of integrals by differentiation with application to collision methods. *Nucl. Sci. Eng.* 55 (1):96–7.

Bitelli, G., and A. Turrin. 1976. Collision method in spherical geometry by escape probabilities. *Nucl. Sci. Eng.* 60 (3):324–6.

Carlvik, I. 1966. Integral transport theory in one-dimensional geometries. Technical report, AE-227. AB Atomenergi. Retrieved from https://www.osti.gov/etdeweb/servlets/purl/20949510

Gross, R., D. Tomatis, and E. Gilad. 2020. High-accuracy neutron diffusion calculations based on integral transport theory. *Eur. Phys. J. Plus* 135 (2):235.

Hébert, A. 2009. *Applied reactor physics*. Québec, Canada: Presses internationales Polytechniques.

Henderson, N. C., and R. Varadhan. 2019. Damped anderson acceleration with restarts and monotonicity control for accelerating em and em-like algorithms. *J. Comput. Graph. Stat.* 28 (4):834–46.

Lawrence, R. D. 1986. Progress in nodal methods for the solution of the neutron diffusion and transport equations. *Prog. Nucl. Energy* 17 (3):271–301.

Lewis, E. E., and W. F. Miller. 1984. *Computational methods of neutron transport*. La Grange Park, IL: American Nuclear Society Inc.

Quarteroni, A., R. Sacco, and F. Saleri. 2007. *Numerical mathematics*. 2nd ed. Berlin, Heidelberg: Springer.

Ronen, Y. 2004. Accurate relations between the neutron current densities and the neutron fluxes. *Nucl. Sci. Eng.* 146 (2):245–7.

Smith, K. S. 1983. Nodal method storage reduction by nonlinear iteration. *Trans. Am. Nucl. Soc.* 44:265–6.

Sood, A., R. A. Forster, and D. Kent Parsons. 2003. Analytical benchmark test set for criticality code verification. *Prog. Nucl. Energy* 42 (1):55–106.

Stamm'ler, R. J. J., and M. J. Abbate. 1983. *Methods of steady-state reactor physics in nuclear design*, vol. 111. London: Academic Press.

Tomatis, D., and A. Dall'Osso. 2011. Application of a numerical transport correction in diffusion calculations. Paper presented at the Proceedings of the International Conference on Mathematics and Computational Methods Applied to Nuclear Science and Engineering (M&C 2011), Rio de Janeiro, Brazil, May 8–12.

Appendix A: Gauss-quadratures

The integrals used in the calculation of the probabilities in the cylindrical and spherical frames are in the form:

$$I = \int_{r_{i-1/2}}^{r_{i+1/2}} dh K(\ell(h)),$$

and they are often evaluated numerically by Gauss-quadrature. The integrand can show an endpoint singularity in the first derivative when integrating in the convex regions, since $d_h K = \partial_\ell K \ \partial_\ell h$ and

$$\lim_{h \to r_{i+1/2}} \frac{-2h}{\sqrt{r_{i+1/2}^2 - h^2}} = -\infty,$$

for $\ell = 2\sqrt{r_{i+1/2}^2 - h^2}$ (Hébert, 2009). The use of a Gauss-Legendre quadrature with N points in the integration interval is a good choice only if the integrand is continuous over the interval up to order $2N$. Gauss-Legendre quadrature integrates exactly polynomials of degree less than $2N$. The definite integrals can be regularized by a proper change of variable following the Flurig scheme, which yields a Gauss-Jacobi quadrature scheme (Carlvik, 1966). We propose hereafter a general change of variable to obtain both schemes at once:

$$\varrho = 1 - 2\left(\frac{r_{i+1/2} - h}{\Delta r_i}\right)^{(1-\alpha/2)} \tag{21}$$

with $\Delta r_i = r_{i+1/2} - r_{i-1/2}$ that yields

$$I = \frac{\Delta r_i}{2}\int_{-1}^{1} d\varrho (1-\varrho)^{\alpha} K(\ell(\varrho)) = \sum_{n=1}^{N} w_n K(\ell(h_n)), \tag{22}$$

with the Gauss-Legendre scheme for $\alpha = 0$ and the Gauss-Jacobi scheme for $\alpha = 1$. After retrieving the weights v_n and the roots ϱ_n of the selected N-point quadrature in $[-1, +1]$, the weights and roots to use in Equation (22) are respectively:

$$w_n = \frac{\Delta r_i}{2} v_n \quad \text{and} \quad h_n = r_{i+1/2} - \left(\frac{1-\varrho_n}{2}\right)^{(1+\alpha)} \Delta r_i. \tag{23}$$

Weights and roots are obtained by the Scipy v1.4.1 library (special.roots_jacobi) and Numpy v1.18.2 (polynomial.legendre.leggauss). We note that the values from these libraries are different from the ones printed in the cited textbooks (Hébert, 2009; Stamm'ler and Abbate, 1983).

Appendix B: Direct solution of integral transport by the collision probability method

The integral transport equation for the scalar flux with isotropic sources can be written using the first flight collision probabilities as (Lewis and Miller, 1984; Hébert, 2009):

$$V_i \sigma_i \phi_i = \sum_{j=1}^{I} q_j V_j \tilde{p}_{ij} + J_b^{(-)} S_b \tilde{p}_{ib}, \tag{24a}$$

where b stands for any boundary with a non-zero entering current $J_b^{(-)} = \phi_b/4$, given as well by an isotropic angular flux. $\tilde{p}_{ij}$ and $\tilde{p}_{ib}$ are the probabilities of a neutron to have its first collision in the volume V_i after being emitted isotropically in the volume V_j or from the surface S_b, respectively. $b = I + 1/2$ for the cylindrical and for the spherical geometries after placing the center at $x_a = 0$ ($a = -1/2$), whereas two incoming currents can be present in the slab. This equation can be simplified further by using the reciprocity property from Equations (19),

$$\phi_i = \sum_{j=1}^{I} q_j p_{ji} + 4 J_b^{(-)} \tilde{e}_{bi} \tag{24b}$$

with the reduced escape probability $p_{ji} = \tilde{p}_{ji}/\sigma_j$ and the escape probability counting for both the signed terms. The incoming current at the boundary can be given as fixed external source, or being expressed as proportional to the out-going current by means of an albedo $0 \leq \beta \leq 1$, like

$$J_b^- = \beta_b J_b^+ = \beta_b \left(\sum_{j=1}^{I} \frac{q_j p_{jb}}{4} + \tilde{r}_b J_b^- + \tilde{t}_{ba} \frac{S_a}{S_b} J_a^+\right), \text{ and} \tag{25a}$$

$$J_a^+ = \beta_a J_a^- = \beta_a \left(\sum_{j=1}^{I} \frac{q_j p_{ja}}{4} + \tilde{r}_a J_a^+ + \tilde{t}_{ab} \frac{S_b}{S_a} J_b^- \right), \tag{25b}$$

with the reduced collision probability from the surface at x_b thanks again to reciprocity. About 19 b, reciprocity always considers entering neutrons distributed according to the cosine described by the direction of flight and the normal to the same surface, yielding a cosine current by $J^{\pm} = \phi/4$, suitable to reproduce white reflection with $\beta = 1$. The reflection $\tilde{r}$ is the probability that a neutron enters the outer surface with the cosine distribution, travels inwards and leaves it back again without colliding. It must be zero in the slab, but not in the cylinder or in the sphere. Transmission is used instead when the leaving surface to be crossed is different from the entering one, and it is non-vanishing here only in the slab. Conservation applied in the cylinder or in the sphere implies that $\tilde{r}_b = 1 - \sum_j \tilde{p}_{jb}$, where we have also assumed implicitly no possible transmission in the derivation of their escape probabilities. Similarly in the slab, it is $\tilde{t}_{ab} = 1 - \sum_j \tilde{p}_{jb}$ for instance. Equation (25b) can be used for Equation (25a) to obtain an expression for J_b^- that is suitable for substitution in Equation (24a). Equations (25) are in a general form for 1D geometries, which simplify either in the slab or in the others.

The source term considers only isotropic emission, and it is composed by scattering and fission production as in Equation (7a). In absence of external sources, the problem becomes homogeneous with the multiplication factor k assuming the role of eigenvalue to avoid the only vanishing solution. Equations (24) hold for any energy group, whose index is dropped for simplicity.

We setup hereafter an algebraic system of equations for the unknown flux array $\vec{\phi}$ of size $(I \times G)$, flattened with the index of the spatial mesh running first. The extension of the solution method to problems with external sources in submultiplicative media is straightforward. Equation (24b) for bare bodies, that is in presence of vacuum boundary condition, is rewritten as:

$$(\mathbf{I} - \mathbf{PS})\vec{\phi}^{(n+1)} = \mathbf{P}(\chi \otimes \mathbf{F})\vec{\phi}^{(n)}/k^{(n)}, \tag{26}$$

where the index n addresses power method iterations to solve the eigenvalue problem. All matrices in Equation (26) are constructed by blocks. $\mathbf{I}$ is the identity matrix. The matrix $\mathbf{P}$ is block diagonal and it is constituted of (transposed) matrices of reduced collision probabilities per group, placed in increasing order from the fast groups, which are assigned to the lowest values of the index g as usual. The matrix $\mathbf{S}$ is composed by $G \times G$ diagonal blocks with elements $[\sigma_{s,g\leftarrow g',j}\delta_{ij},\ i,j = 1,\ldots,I]$, contrary to the matrix $\mathbf{F}$ which has only G blocks set by columns and with elements $[\nu\sigma_{f,g,j}\delta_{ij},\ i,j = 1,\ldots,I]$. The new estimate of the flux vector is computed by multiplying the left side of the equation by the inverse of the removal matrix, i.e. $(\mathbf{I} - \mathbf{SP})^{-1}$, assuming that it is invertible. The new estimate of the eigenvalue can be obtained by enforcing neutron conservation through the iterations, while achieving the convergence:

$$k^{(n+1)} = k^{(n)} \frac{\langle \vec{\phi}^{(n+1)} | \mathbf{F}\vec{\phi}^{(n+1)} \rangle}{\langle \vec{\phi}^{(n+1)} | \mathbf{F}\vec{\phi}^{(n)} \rangle}.$$

The full eigen-spectrum can be obtained by resolving the problem for the fission production reaction rates, showing smaller rank. First, note that $(\chi \otimes \mathbf{F}) = \mathbf{XF}$, with $\mathbf{X}$ built by G diagonal blocks stacked per row of the form $[\chi_{g,j}\delta_{ij},\ i,j = 1,\ldots,I]$. The eigen-solver operates then on the matrix $\mathbf{F}(\mathbf{I} - \mathbf{SP})^{-1}\mathbf{PX}$.

In case the partial current is given by an albedo relation at the boundary of the cylinder (or of the sphere), the same solving scheme still holds after redefinition of the matrix **P**:

$$\mathbf{P} \leftarrow \mathbf{P} + \frac{\beta_b}{1 - \beta_b \tilde{r}} \mathbf{E}_b,$$

with $\mathbf{E}_b = [\tilde{e}_{bi} p_{jb},\ 1 \leq i,j \leq I]$. This redefinition holds also for the slab in case of periodic boundary condition, i.e. $J_b^- = J_a^+$. Lastly for the slab, a general relation for the right boundary is

$$\mathbf{P} \leftarrow \mathbf{P} + \frac{\beta_b}{1 - \beta_a \beta_b \tilde{t}^2} \left(\mathbf{E}_b + \beta_a \tilde{t} \mathbf{E}_a \right)$$

with $\mathbf{E}_a = [\tilde{e}_{bi} p_{ja},\ 1 \leq i,j \leq I]$. The corresponding expression at the left boundary is easy to obtain.